



Impacts of solar-absorbing aerosol layers on the transition of stratocumulus to trade cumulus clouds

Xiaoli Zhou¹, Andrew S. Ackerman², Ann M. Fridlind², Robert Wood³ and
Pavlos Kollias^{4,5}

1. Department of Atmospheric and Oceanic Sciences, McGill University, Montreal,
Quebec, CA
2. NASA Goddard Institute for Space Studies, New York, New York, USA
3. University of Washington, Seattle, Washington, USA
4. School of Marine and Atmospheric Sciences, Stony Brook University, Stony Brook, New
York, USA
5. Department of Environmental and Climate Sciences, Brookhaven National Laboratory,
Upton, New York, USA

Correspondence to: Xiaoli Zhou (xiaoli.zhou@mail.mcgill.ca)



Abstract

The effects of an initially overlying layer of solar-absorbing aerosol on the transition of stratocumulus to trade cumulus clouds are examined using large-eddy simulations. The transition of lightly drizzling cloud is generally hastened, resulting mainly from increased 5 cloud droplet number concentration (N_c) induced by entrained aerosol. The increased N_c slows sedimentation of cloud droplets and shortens their relaxation time for diffusional growth, both of which accelerate entrainment of overlying air and thereby stratocumulus breakup. However, the decrease in albedo from cloud breakup is more than offset by redistributing cloud water over a greater number of droplets, such that the diurnal-average 10 shortwave forcing at the top of atmosphere is negative. The negative radiative forcing is enhanced by sizable longwave contributions, which result from the greater cloud breakup and a reduced boundary layer height associated with aerosol heating. A perturbation of moisture instead of aerosol aloft leads to greater liquid water path and a more gradual transition. Adding absorbing aerosol to that atmosphere results in substantial reductions 15 in LWP and cloud cover that lead to positive shortwave and negative longwave forcings on average canceling each other. Only for heavily drizzling clouds is the breakup delayed, as inhibition of precipitation overcomes cloud water loss from enhanced entrainment. Considering these simulations as an imperfect proxy for biomass burning plumes influencing Namibian stratocumulus, we expect regional indirect plus semi-direct 20 forcings to be substantially negative to negligible at the top of atmosphere, with its magnitude sensitive to background and perturbation properties.



1. Introduction

25 Aerosols affect the earth's radiation budget in at least three ways. First, they directly absorb and scatter solar radiation. Second, they affect radiative fluxes indirectly through their role as cloud condensation nuclei, influencing cloud microphysics and thereby affecting cloud albedo and cloud cover. Third, solar-absorbing aerosols can alter atmospheric heating rates and stability, leading to rapid adjustments in cloud properties; 30 the resulting impact on radiative fluxes is referred to as the semi-direct effect (Hansen et al., 1997).

 Aerosols have been identified as contributing the greatest uncertainty to anthropogenic climate forcing (Forster et al. 2007). For instance, with regard to semi-direct forcings, some general circulation model (GCM) studies (e.g., Hansen et al., 1997; 35 Lohmann and Feichter, 2001; Jacobson, 2002; Cook and Highwood, 2004) have found a net decrease in low-level cloud cover, which corresponds to a positive radiative forcing at the top of the atmosphere (TOA) that tends to warm the climate system, while others (e.g., Menon et al., 2002, Penner and Zhang, 2003; Sakaeda et al, 2011) have found the opposite, in which the cloud water increases and the radiative forcing depends crucially 40 on the height of the absorbing aerosol. To better constrain radiative forcing in climate models, a comprehensive understanding of regional cloud-aerosol interactions and the corresponding radiative forcings is of value.

 Here we focus on warm (liquid-phase) clouds in the planetary boundary layer (PBL). Process-level understanding of the physical mechanisms underlying indirect and 45 semi-direct aerosol radiative forcings has been largely advanced through studies with large-eddy simulation (LES) models and in situ observations. Regarding aerosol indirect



forcing, with all else equal (particularly cloud cover and liquid water path), increased cloud droplet number concentration (N_c) resulting from increased aerosol concentration (N_a) increases cloud optical thickness and thus albedo, thereby exerting a negative radiative forcing at TOA (Twomey 1974, 1991). For precipitating clouds, increasing N_c can reduce precipitation and thereby enhance liquid water path (LWP) and cloud cover (e.g., Albrecht, 1989; Ackerman et al., 1993; Pincus and Baker, 1994; Hindman et al., 1994). However, for clouds with little precipitation, modeling studies indicate that increased N_c tends to reduce LWP and cloud cover by increasing PBL entrainment (Ackerman et al., 2004; Wood et al., 2007; Ackerman et al., 2009), which can dry the PBL and reduce LWP when the overlying air is sufficiently dry (Randall, 1984). Such a tendency is consistent with satellite observations of LWP reduction in ship tracks, on average (Coakley and Walsh, 2002). At least three microphysical mechanisms have been found to play a role in the entrainment increase. First, in what we shall refer to as the "sedimentation effect", increased N_c leads to smaller droplets that fall more slowly, which increases the amount of cloud water available for evaporative cooling during entrainment events, thereby strengthening entrainment (Bretherton et al., 2007). Second, in what we shall refer to as the "evaporation effect", smaller droplets increase the total surface area of cloud droplets, accelerating evaporation and driving stronger entrainment (Xue et al., 2008). Third, increased N_c also suppresses drizzle, enhancing convective intensity and entrainment (e.g., Stevens et al. 1998, Wood et al. 2007). Under dry overlying air, all three effects tend to reduce cloud cover and LWP, leading to a positive radiative forcing. However, if the entrained air is sufficiently moist, entrainment can be expected to increase LWP (Randall, 1984).



70 Aerosol semi-direct effects have been studied by Ackerman et al. (2000) in the context of trade cumulus under a sharp inversion, in which absorbing aerosol within the boundary layer increases solar heating in a manner that stabilizes the PBL, reducing the moisture supply from the surface and the amount of cloudiness, leading to a positive radiative forcing at TOA. More directly in such a scenario the relative humidity of the
75 PBL is reduced by enhanced solar heating, reducing cloudiness as originally found in global model simulations by Hansen et al. (1997). In contrast, Johnson et al. (2004) conducted large-eddy simulations of marine stratocumulus and found that an absorbing aerosol immediately above the PBL (and not entrained) strengthens the inversion, reducing entrainment and thereby increasing cloud cover, leading to a negative radiative
80 forcing, while they found the opposite (positive radiative forcing) for aerosol heating within the PBL. That study was motivated at least in part by measurements of absorbing aerosol from biomass burning advected from Africa over Namibian stratocumulus, where biomass burning aerosol plumes may also be well separated from the PBL (Keil and Haywood, 2003, Haywood et al., 2003b), a factor that has been found to be critical to
85 absorbing aerosol effects on cloud fraction (Feingold et al., 2005).

Further complexity arises when considering the possibility that absorbing aerosol can act as cloud condensation nuclei (CCN) and thereby increase N_c , which was neglected in the early studies of Johnson et al. (2004) and Feingold et al. (2005) and only represented quite crudely by Ackerman et al. (2000), who simply imposed a sequence of
90 uniform N_c values in their simulations. Here we will consider both roles of absorbing aerosol.



By considering two trade cumulus regimes, one transitional case with a sharp inversion (ATEX) and a more downstream case with greatly reduced cloud cover (BOMEX), Johnson (2005) found the semi-direct aerosol forcing to depend strongly on 95 the cloud regime, with the magnitude of the forcing increasing with (unperturbed) cloud cover. This regime dependence is relevant to the stratocumulus-to-cumulus transition (SCT), a climatological feature downstream of subtropical marine stratocumulus (Klein and Hartmann, 1993; Sandu et al., 2010; Zhou et al., 2015). The SCT has been found in modeling studies to be driven by equatorward advection over increasing sea surface 100 temperatures (SST), which increases surface latent heat fluxes, enhancing buoyancy fluxes in the cloud layer and hence entrainment. The PBL deepening from progressive entrainment inhibits the ability of circulations forced at cloud top to maintain a well-mixed boundary layer, reducing the surface moisture supply and eventually drying out the stratocumulus clouds (Bretherton and Wyant, 1997; Wyant et al., 1997). A recent 105 observational study has found that the time scale of the SCT over the eastern Pacific can depart considerably from that in an idealized model framework driven only by increasing SST (Zhou et al., 2015), suggesting that other factors, such as meteorological variability, might play important roles in the time scale of SCT. Yamaguchi et al. (2015) (hereafter Y15) investigated the impact of overlying absorbing aerosol and associated enhanced 110 moisture on the SCT and found that entrained absorbing aerosol in general delays the SCT with a net negative change in TOA shortwave (SW) cloud radiative forcing (CRF).

It has been documented in recent observational studies near northern Namibia and remote St. Helena Island in the South Atlantic Ocean that the sampled absorbing aerosol is often accompanied by enhanced humidity, with an average moisture perturbation of



115 $\sim 1 \text{ g kg}^{-1}$ relative to the underlying air (Haywood et al., 2003b; Adebiyi et al. 2015). This
humidity is associated with the outflow from the deep, continental boundary layer. The
enhanced humidity induces additional radiative heating, which can regulate cloud
processes by reducing cloud-top longwave (LW) cooling (Adebiyi et al. 2015; hereafter
A15) and by simply reducing the dryness of air entrained into the PBL. Y15 located a
120 stationary moist layer above the PBL and found that the additional moisture itself
enhances cloud breakup during the SCT, although they acknowledge that their
perturbation of $\sim 3 \text{ g kg}^{-1}$ likely represents an upper limit compared with A15.

Here we perform an expanded investigation of the impact of absorbing aerosol
and moisture on the SCT. Because Y15 was published during the course of this work, our
125 simulation setups are similar but not identical, and we highlight similarities and
differences below. Like Y15, we adopt the Sandu and Stevens (2011) SCT case study,
with some modifications. Here we separate the responses to aerosol heating above and
within the PBL and on microphysical processes. We consider the impacts on lightly and
heavily drizzling stratocumulus decks. We also assess the impacts of additional overlying
130 moisture on the SCT and how it influences the effects of absorbing aerosol. The radiative
forcings in our study consider not only changes in SW but also LW fluxes. Our results
differ from Y15 in that initially overlying plumes of absorbing aerosol lead to positive
changes in SW CRF at TOA, and the aerosol and moisture perturbations never delay the
SCT in our simulations (unless we omit well-established physical processes).

135 The remainder of this manuscript is organized as follows. Section 2 documents
the model setup and case description. Section 3 presents analysis of the microphysical
and heating effects of absorbing aerosol during the transition of lightly drizzling



stratocumulus. In sect. 4, we investigate the impact of additional moisture in the aerosol layer, and the influence of the initial altitude of the moist aerosol layer. The impacts of an 140 absorbing aerosol on the SCT of heavily drizzling stratocumulus are discussed in sect. 5. In sect. 6 we discuss and summarize our findings.

2. Model setup and simulated cases

The Distributed Hydrodynamic Aerosol and Radiative Modeling Application 145 (DHARMA) (Ackerman et al., 2004 and references therein) simulations here are based on the "reference case" 3-day Lagrangian SCT setup of Sandu and Stevens (2011). The basis for the case is a composite of the large-scale conditions encountered along trajectories over the northeast Pacific from June to August of 2006 and 2007. An intercomparison of six different LES models shows that DHARMA results are consistent 150 with others in representing the SCT (de Roode et al., 2016), although differences between models do exist, as discussed further below. Unlike Sandu and Stevens (2011) and Y15, here we begin simulations at midnight local time (when turbulent mixing is vigorous, to accelerate spin-up) rather than 10:00 local time.

The DHARMA domain size is 10.8 km x 10.8 km x 3.2 km and horizontal 155 resolution is set to $\Delta x = \Delta y = 75$ m. Vertically 240 levels are distributed between 0 and 3200 m, with variable vertical resolution ranging from 30 m near the surface to 10 m near the inversion and up to 60 m near the model top; before using this grid with twice as coarse of a grid as in de Roode et al. (2016), we confirmed that the DHARMA results were not sensitive to the difference. The microphysics scheme is an adaptation of the 160 two-moment scheme of Morrison et al. (2005) with prognostic saturation excess



following Morrison and Grabowski (2008) and assuming the shape factor of the cloud droplet size distribution to be 10.3 (equivalent to relative dispersion of 0.3) following Geoffroy et al. (2010). Activation of aerosol follows Abdul-Razzak and Ghan (2000) using supersaturation computed after the condensational adjustment of Eq. A10 in

165 Morrison and Grabowski (2008). The aerosol are semi-prognostic: prognostic in that the number concentration of unactivated plus activated aerosol for each species is prognostic (advection), but there is no evolution of the size and breadth of the underlying aerosol size distribution for each species nor are there sources or sinks of aerosol number, and thus the scheme is diagnostic in the sense that total particle number concentration is conserved.

170 Two species of aerosol are prescribed: ammonium sulfate and a solar-absorbing aerosol; both aerosol types act as CCN and interact with the radiation before and after activation. The baseline case is an ensemble of three simulations with different pseudo-random seeds for the initial temperature perturbation field in the PBL, and includes only ammonium sulfate aerosol, which are uniformly distributed in the vertical with

175 $N_{a, \text{sulfate}} = 150 \text{ mg}^{-1}$ (without a vertical gradient the aerosol scheme is completely diagnostic). Further simulations are conducted that incorporate an absorbing aerosol profile initialized to increase linearly from zero below 1250 m altitude up to $N_{a, \text{absorb}} = 5000 \text{ mg}^{-1}$ at 1300 m, maintain a uniform value up to 2800 m, then decrease to zero at 2850 m and above. Log-normal size distributions are specified for the sulfate and

180 absorbing aerosol, with geometric mean radii of 0.05 μm and 0.12 μm and geometric standard deviations of 1.2 and 1.3, respectively. The hygroscopicity parameter κ (Petters and Kreidenweis, 2007) is set to 0.55 for ammonium sulfate and 0.2 for the absorbing aerosol. The size distribution for the absorbing aerosol is based on the measurements of



Haywood et al. (2003b) and the hygroscopicity (for aged biomass burning aerosol) from
185 those of Englehart et al. (2012). The absorbing aerosol optical properties follow the approach of Ackerman et al. (2000) but here a soot core radius of $0.04\text{ }\mu\text{m}$ is specified, resulting in a single scattering albedo (SSA) of 0.88 at wavelength $0.55\text{ }\mu\text{m}$. The extinction coefficient within the absorbing aerosol layer is about 0.16 km^{-1} at $0.55\text{ }\mu\text{m}$, consistent with the measurements reported by Haywood et al. (2003a). The absorbing
190 aerosol induces a heating rate of $\sim 2.6\text{ K d}^{-1}$ at noon and a diurnal-average heating rate $\sim 1.2\text{ K d}^{-1}$, consistent with observations exploited by Johnson et al. (2004) and Ackerman et al. (2000). The initial absorbing aerosol layer physical thickness of 1.5 km is loosely based on observations over the southeast Atlantic by Chand et al. (2009), Haywood et al. (2003b), and Labonne et al. (2007), who report characteristic layer thickness over the
195 Atlantic of 1 to 2 km. Sensitivities of the results to the assumed SSA of the absorbing aerosol and to their initial number concentration are briefly discussed.

To examine variations in bulk properties of the overlying aerosol layer, a further simulation is performed with the initial location 400 m higher, in which the model domain is extended to 3.5 km and the column of overlying water vapor and ozone used
200 for radiative fluxes adjusted accordingly. An additional baseline case with a 3.5-km deep grid was run for computing differences. Two other simulations consider a moist perturbation of 1 g kg^{-1} based on observations at St. Helena Island of outflow from the continental boundary layer (A15), scaled to the initial height of $N_{\text{a,absorb}}$ with and without absorbing aerosol. Finally, the impact of overlying absorbing aerosol on heavily
205 precipitating stratocumulus is examined by reducing $N_{\text{a,sulfate}}$ to 25 mg^{-1} . To isolate the microphysical effects of the overlying aerosol, a group of simulations is performed where



the interaction of the absorbing aerosol with radiation is omitted. The aforementioned sedimentation and evaporation effects are examined by additional simulations that exclude cloud droplet sedimentation and that fix the cloud droplet relaxation time scale
210 (instead of computing it per Equation A5 of Morrison and Grabowski, 2008). Semi-direct aerosol effects are dissected through simulations that restrict aerosol heating to the free troposphere (FT) or the PBL.

Radiative forcings are computed from hourly time slices, which yield daily averages that differ negligibly from those using radiative fluxes updated every minute.
215 We compute aerosol forcings following Ghan (2013), in which total forcing from a perturbation is calculated as the change in net downward radiative flux at TOA relative to the baseline: $\Delta F = F(\text{perturbed}) - F(\text{baseline})$. The sum of the indirect and semi-direct forcings from the absorbing aerosol is computed similarly but with the absorbing aerosol omitted when calculating $F(\text{perturbed})$. The direct aerosol forcing is then derived by
220 subtracting the sum of indirect and semi-direct forcings from the total forcing.

For the sake of comparison with Y15, in one instance we also compute cloud radiative forcing as the difference of net downward radiative fluxes at TOA with and without cloud: $F(\text{all sky}) - F(\text{clear sky})$. The difference between ΔF and the aerosol-induced change in cloud radiative forcing is the direct aerosol forcing for clear sky:
225 $\Delta \text{ACRF} = \Delta F - \Delta F(\text{clear sky})$. The enhancement of aerosol absorption associated with SW reflection by an underlying cloud layer, which tends toward a positive forcing (e.g., Chand et al., 2009) and is implicitly included in ΔF , is offset in ΔACRF by the subtraction of a direct forcing that tends more negative here, because the ocean surface is less



reflective than the cloud layer. Subtraction of a negative direct forcing thereby yields a
230 ΔCRF that tends to be more positive than total forcing ΔF .

In all forcing calculations for this study, net LW fluxes at TOA are scaled from net LW fluxes at the top of the model domain using $F_{\text{TOA}} = 2.627F_{3.2\text{km}} + 0.0054F_{3.2\text{km}}^2$ for the 3.2-km deep grid, and using $F_{\text{TOA}} = 2.469F_{3.5\text{km}} + 0.0046F_{3.5\text{km}}^2$ for the 3.5-km deep grid. These correlations were derived from the baseline case run on a 40-km deep
235 grid, with root mean square (RMS) errors of 0.3 and 0.2 W m^{-2} on the shallower grids, with biases of less than 0.001 W m^{-2} . No TOA corrections for SW fluxes are made because the radiative transfer scheme (Toon et al., 1989) provides accurate TOA fluxes by treating Rayleigh scattering in the overlying atmosphere.

240 3. Impacts on lightly drizzling SCT

3.1. Overview of SCT with and without absorbing aerosol layer

Figs. 1 and 2 illustrate the transition from a compact stratocumulus layer to more broken fields of cumulus as a response to increasing SST for the lightly drizzling baseline case ($N_{\text{a, sulfate}} = 150 \text{ mg}^{-1}$, $N_c \sim 100 \text{ cm}^{-3}$). The PBL depth in general increases with SST
245 and reaches 2 km at the end of day 3 (Fig. 1a). The thinning of the stratocumulus is observed in the afternoon of day 1 as solar heating offsets some of the LW cooling that drives PBL mixing, when vertical wind variance profiles show bimodal structure with a local minimum near cloud base ($\sim 12 \text{ h}$ in Fig. 1b). Convection revitalizes after sunset and deepens the stratocumulus. Starting around sunrise of day 2 ($\sim 30 \text{ h}$), the PBL becomes
250 continuously stratified, with a persistent cumulus layer developing under the stratocumulus (Fig. 1a). This stratification reduces the subsequent nocturnal recovery,



and leads to further reduction in LWP (Fig. 2b) and cloudiness (Fig. 2c) after sunrise on day 3. Following Sandu and Stevens (2011) by defining the SCT as the time at which cloud cover (the fraction of columns with $LWP > 10 \text{ g m}^{-2}$) first decreases to half of its
255 initial value, the transition in the baseline case is at $\sim 62 \text{ h}$.

When incorporating an overlying absorbing aerosol layer, the clouds and PBL evolve in a notably different way with an evident radiative impact (Figs. 2 and 3; Table 1). N_c increases gradually after the bottom of the ramp of subsiding aerosol contacts the deepening PBL at $\sim 15 \text{ h}$ (Fig. 2a). The full strength of the aerosol layer reaches the PBL
260 at $\sim 20 \text{ h}$ (Fig. 2d). Before the subsiding aerosol layer contacts the deepening PBL, absorption of SW radiation in the aerosol layer dominates the radiative impact and reduces the diurnal-average upwelling SW radiative fluxes at TOA by $\sim 7 \text{ W m}^{-2}$ on day 1 (Fig. 2f, Table 1). This SW absorption by the aerosol layer decreases with time when the cloud field is more broken, since less upwelling SW radiation is reflected back into the
265 layer (cf. Chand et al., 2009) and when it is mixed below cloud, where less SW radiation reaches the absorbing aerosol. On day 3, SW absorption is overcome by scattering, resulting in a negative direct forcing (Table 1).

As the absorbing layer approaches the PBL, the inversion strengthens (Fig. 2h), which would tend to slow entrainment. However, as the layer makes contact with the
270 clouds, the entrained aerosol activate cloud droplets and lead to a pronounced increase of N_c , which is ultimately increased by a factor of ~ 10 over the baseline to $\sim 1000 \text{ cm}^{-3}$ (Fig. 2a). The increased N_c acts to accelerate entrainment through the sedimentation and evaporation effects, and opposes but does not overcome the opposing tendency from the strengthening of the inversion (Figs. 2d and 2e). The entrainment of warmer air with less



275 RH leads to a reduction of LWP (Fig. 2b) and cloud cover (Fig. 2c), hastening and
enhancing the SCT on day 2 (Fig. 2c). This SCT acceleration is opposite to Y15 who
found that entrained absorbing aerosol delays the SCT and leads to overcast conditions
during the second half of 72-h simulations. As a result of substantially reduced LWP,
here the overlying absorbing aerosol case yields a positive change in TOA SW CRF
280 relative to the baseline during the 3-day simulation (Table 2). The daytime average SW
 Δ CRF after the soot contacts the PBL is 9.3 W m^{-2} , opposite in sign to that of Y15.
Meanwhile, the negative LW contributions to Δ CRF are enhanced during the transition,
and overcome the positive SW Δ CRF on day 3. As explained further below, such LW
contributions result from microphysical and heating effects. While such LW forcings are
285 often ignored when considering aerosol impacts on low-lying clouds, much of the
subtropical and tropical atmosphere is not particularly moist, with column water vapor of
less than 30 mm (cf. Lindstrot et al. 2014) as it is here (initial and final values
respectively about 25 and 30 mm), allowing changes in low-level clouds to impact LW
fluxes at TOA.

290

3.2 Microphysical effects

The microphysical effects of the subsiding aerosol are isolated by omitting aerosol
heating and comparing to the same baseline (Fig. 4). The substantial increase of N_c as a
result of the entrained aerosol is seen to largely explain overall reductions of both LWP
295 and cloud cover relative to the baseline simulation, leading to a hastened SCT. Such
disparity in LWP and cloud cover with and without entrained aerosol is reduced when
either the sedimentation effect is excluded (by omitting cloud droplet sedimentation from



both simulations) or when the evaporation effect is excluded (by fixing the cloud droplet diffusional growth relaxation time in both simulations). When both effects are excluded,
300 simulations with and without entraining aerosol exhibit negligible differences in LWP and a reversed difference in cloud cover. Thus, the hastened SCT from absorbing aerosol in DHARMA simulations can be attributed primarily to the microphysical effects of increased N_c , specifically via sedimentation and evaporation effects.

With the semi-direct effect now excluded by omitting aerosol absorption, the
305 indirect forcing is isolated (Table 3). Despite the substantial reduction in cloud cover, the entrained aerosol results in only a modest positive aerosol indirect forcing on day 2 and a negative forcing on day 3 (Table 3). The negative forcing is driven by a negative LW forcing, as a result of more broken clouds and emission from a warmer SST, and by a significant Twomey effect, which does not fully offset the opposed, comparable SW
310 forcing induced by the sedimentation and evaporation effects (Table 4).

3.3 Semi-direct effect

Next we isolate the semi-direct effect of aerosol heating by considering aerosol absorption in the FT, PBL and throughout the atmosphere and comparing to the
315 preceding case that only included microphysical effects of the entrained aerosol layer. As seen in Fig. 5, aerosol heating in the FT substantially strengthens the PBL inversion as the aerosol layer approaches the PBL (Fig. 5e), enhancing LWP and cloud cover (Figs. 5b and 5c) by inhibiting entrainment (Fig. 5d). The increase of LWP delays and weakens the SCT, contributing to a negative SW forcing (Table 5). In contrast, aerosol heating in the
320 PBL reduces LWP and cloud cover in the daytime (Figs. 5b and 5c) by lowering the



relative humidity in the PBL and by stabilizing the PBL (Fig. 6a), hampering the moisture supply from the surface (Fig. 6b). The reduction in cloud amount amplifies the diurnal contrast of cloud fraction and hastens the SCT, resulting in a positive SW forcing (Table 5).

325 The competing effects of aerosol heating in the FT versus the PBL serve to increase cloud water at night while reducing it during daytime, enhancing its diurnal cycle (Fig. 5c). Diurnally averaged, the effect of aerosol heating in the FT is dominant and leads to increased LWP and cloud cover and therefore a negative average SW forcing during the 3-day transition (Fig. 5c, Table 5). The net SW forcing is smaller than the sum
330 of the SW forcings via individual FT and PBL aerosol heating, indicating interactions that reduce the component forcings when combined (Table 5). Specifically, aerosol absorption in the FT slightly reduces the SW flux available for aerosol heating in the PBL, while the greater cloud breakup in the daytime reduces the reflected upwelling SW flux, in turn reducing aerosol heating in the FT. The combined effects also result in LWP and
335 cloud cover intermediate between the results when considered separately (Fig. 5).

340 In contrast to the counteracting impacts on cloud water, FT and PBL aerosol heating both inhibit entrainment by intensifying the inversion and by stratifying the PBL (Fig. 5c). The reduced PBL depth corresponds to warmer cloud tops, which emit more LW radiation upwards, leading to net negative LW forcing on days 2 and 3 despite an increase of LWP and cloud cover (Table 5).



3.4. Combined effects

Comparing Tables 1, 3 and 5 it is seen that net SW forcing is weakened with all effects included because the increased LWP from aerosol heating compensates for some 345 of the LWP loss from microphysical effects on day 2 (Table 1, Fig. 6), and the direct aerosol heating on day 1 greatly counteracts the negative radiative forcings after the aerosol layer contacts the PBL. As a result, the mean SW impact over the 3-day transition nearly vanishes (Table 1). The LW radiative forcing, however, accumulates and strengthens during the transition, and therefore is the dominant contributor to a negative 350 average forcing during the transition (Table 1). In a nutshell, although the subsiding aerosol layer directly absorbs solar radiation and breaks up the clouds faster and more thoroughly, the CCN source serves to distribute cloud water over a greater number of drops, increasing the optical thickness of the remaining clouds but at a lower altitude, increasing both upwelling SW and LW radiative fluxes, leading to a net negative forcing. 355 We note that day 3 net SW forcing is only negative when the aerosol is absorbing (-1.2 W m⁻² in Table 1); otherwise, the Twomey effect is not strong enough to counteract the reduction in cloud fraction and day 3 net SW forcing is equally positive (1.2 W m⁻² in Table 3).

The study of the effects of absorbing aerosol on the SCT by Y15 considered only 360 SW forcings, which seems sensible given that studies of semi-direct effects in stratocumulus (Johnson et al., 2004) and trade cumulus (Ackerman et al., 2000; Johnson, 2005) have found SW forcings to be dominant. However, here we find interactions of aerosol and clouds in response to multiple effects leads to small net SW forcings: for example, positive SW forcing from PBL aerosol heating and microphysical effects on



365 dynamics offset negative SW forcing from FT aerosol heating and the Twomey effect (Table 4). By contrast, the negative LW forcings from multiple effects (i.e., cloud water reduction and PBL deepening) work in the same direction and result in a substantial net LW forcing for the SCT.

Sensitivity tests with varying values of the SSA and initial number concentration 370 of the absorbing aerosol are summarized in Appendix A1. A decrease of SSA at 0.55- μm wavelength from 0.88 to 0.71 hastens the SCT less but leads to a positive radiative forcing averaged over the 3-day transition, attributable to direct absorption by the aerosol. A decrease of the initial number concentration for the overlying aerosol with SSA of 0.88 serves to weaken its negative 3-day average radiative forcing.

375

4 Variations in bulk properties of overlying aerosol layer

4.1. Higher initial elevation

Increasing the initial height of the base of aerosol layer by 400 m delays contact 380 with the PBL by about half a day (Fig. 7a). The delayed contact reduces the entrainment of aerosol relative to the case with the layer starting lower, thereby hindering cloud breakup (comparing Figs. 7b-c with Figs. 2b-c). The enhanced cloud amount leads to a much greater SW negative forcing on days 2 and 3, despite greater direct absorption owing to the extended duration of the aerosol aloft on day 2 (Tables 1 and 6). The delayed contact also provides for a longer duration of heating aloft and thereby a stronger 385 inversion on day 3 (Fig. 7e), favoring maintenance of the clouds and thus a negative SW forcing. Despite increased LWP and cloud cover, the SCT with a higher elevated aerosol layer is still hastened relative to the baseline (Fig. 7). The greater negative SW forcing of



the more elevated aerosol layer after its contact with the PBL ultimately leads to a more negative 3-day mean radiative forcing to the case with the layer starting lower (Tables 1
390 and 6).

4.2. Additional moisture

Given that observations indicate that biomass burning plumes over Namibian stratocumulus are moister than the surrounding air (A15), next we additionally consider a
395 moisture perturbation relative to the baseline. As seen in Fig. 8, the moisture induces additional SW heating and LW cooling (Figs. 8a, b), with the latter dominating. The net cooling offsets some SW heating especially near the top of the moist layer (Fig. 8c). Before the moist layer contacts the PBL, the additional downward LW radiative fluxes from its moisture serve to reduce cloud-top radiative cooling and thereby drive weaker
400 PBL mixing that results in a more broken cloud field relative to the dry case (Fig. 9c). Reduced LWP diminishes upwelling SW radiative fluxes, enhancing the positive SW forcing on day 1 (Table 7). After the moist layer contacts the PBL, the entrained moist air leads to greater LWP and cloud cover than for the baseline, despite a weaker inversion
405 (Figs. 8c and 9e). The increased cloud water greatly increases the net outgoing SW flux at TOA on days 2 and 3 (Table 7), and delays the SCT relative to the dry baseline (Figs. 9b and 9c). The SW changes in TOA radiative fluxes are seen in Table 7 to dominate the
410 LW changes.

When an absorbing aerosol is then added to the moist layer aloft, the SCT is faster and more pronounced relative to the case with only a moisture perturbation (Fig. 9c).
410 Comparison of Tables 1 and 8 reveals that the LW forcings are comparable with and



without the additional moisture, but the SW forcings induced by indirect and semi-direct effects are about 4 W m^{-2} greater on days 2 and 3 with the moisture aloft. A thicker cloud layer with greater cloud cover has more to lose, and the more dramatic reduction in cloud cover during daytime predominantly changes the SW forcing. During nighttime, however, 415 cloud cover diminishes less as a result of the entrained moist air (Fig. 9c). The counteracting day and night impacts on cloud cover keep the PBL depth close to that in the absence of the additional moisture (Fig. 9d), leading to little difference in the diurnal average LW forcing (Fig. 9f, Table 8). The net result averaged over the 3-day transition is a modest positive SW forcing that cancels out the negative LW forcing (Table 8).

420

5. Impacts on heavily drizzling stratocumulus

The background aerosol concentrations in our simulations result in negligible drizzle for these conditions. As SCT is often observed in association with precipitation (e.g., Zhou et al., 2015), we next consider the impact of absorbing aerosol on the SCT of 425 heavily drizzling stratocumulus by reducing the $N_{\text{a, sulfate}}$ by six-fold, to 25 mg^{-1} . Throughout this section the aerosol layer base is initially at 1.3 km and the layer does not include additional moisture.

With drizzle the stratocumulus deck retains the essential features of the PBL growth and of the thinning and dissipation of the stratocumulus layer during the SCT, but 430 exhibits differences associated with a much weaker diurnal cycle (Fig. 10), as also reported by Sandu and Stevens (2011). As discussed in Sandu et al. (2008), a weaker diurnal cycle is attributable to depletion of cloud water and stratification of the PBL via precipitation, which limits the stratocumulus invigoration during the night. A reduced



LWP in turn lessens solar heating after sunrise, reducing daytime cloud thinning and
435 breakup.

As seen in Fig. 10, entrainment of aerosol inhibits drizzle and thereby thickens the stratocumulus layer. This inhibition of drizzle restores more than enough cloud water to overcome PBL drying tendencies from the increased entrainment on day 2. After sunrise, cloud cover falls sharply as the reduced drizzle strengthens the diurnal cycle. Owing to a
440 thicker nocturnal cloud deck and a stronger inversion from aerosol heating aloft, cloud breakup is delayed but amplified on day 2. On day 3, the aerosol heating in the presence of a stronger diurnal cycle results in a hastened SCT.

The inhibition of drizzle on day 2 allows for greater mixing and entrainment (cf. Stevens et al., 1998) despite the stronger inversion from aerosol heating aloft (Fig. 10d).
445 The deeper PBL is associated with cooler cloud tops that emit less LW radiation, leading to a positive LW forcing during the transition (Table 9). Such positive LW forcing is more than offset by the strong SW forcing attributable to a strong Twomey effect (relative to a cleaner baseline for this heavily drizzling case), and the net impact is therefore an amplified negative forcing (Table 9).

450

6. Discussion and conclusions

In this study we have examined the impact of an initially overlying layer of absorbing aerosol on the stratocumulus-to-cumulus transition (SCT) of lightly and heavily drizzling clouds via large-eddy simulations. Our results indicate that the
455 overlying aerosol can profoundly modify the breakup of stratocumulus as it advects over increasingly warm SSTs. During the transition of lightly drizzling clouds, an overlying



absorbing aerosol results in a more broken cloud field, hastening the SCT and strengthening the diurnal cycle. The hastened SCT in our simulations is primarily attributable to an increased number concentration of cloud droplets leading to faster 460 evaporation of more cloud water that enhances entrainment. This result holds in the presence of additional moisture in the aerosol layer and is insensitive to a 400-m increase in its initial altitude. Drizzle constitutes another degree of complexity. Its inhibition from aerosol entrainment thickens the stratocumulus and leads to a stronger diurnal cloud cycle that ultimately hastens the SCT.

465 The hastening of the SCT in this study is notable in contrast with Y15, who found the opposite in a similar study. The entrained aerosol in that study leads to increased cloudiness and a delay of the SCT before precipitation develops, suggesting that inhibition of precipitation is not the cause of delayed SCT in Y15. The strength of sedimentation and evaporation effects in the Y15 simulations are not obvious; we do find 470 a delay in the SCT for a lightly drizzling case only when sedimentation and evaporation effects are both omitted (see Appendix A2). It is noteworthy that direct numerical simulation (DNS) indicates that the sensitivity of cloud-top entrainment is substantially underpredicted in LES (de Lozar and Mellado, 2016), so in reality the microphysical effects may be considerably stronger than represented here. Another likely source of 475 discrepancy between our studies could be differences in model formulations. Y15 use the System for Atmospheric Modeling (SAM; Khairoutdinov and Randall, 2003) whereas here we use DHARMA (Ackerman et al., 2004). As seen in the intercomparison of de Roode et al. (2016), the evolution of cloudiness in SAM and DHARMA for that study's reference case (after Sandu and Stevens, 2011, from the observational study of Sandu et



480 al., 2010) is notably different in that DHARMA tends to ultimately develop a more broken cloud field than SAM. The cloud cover in DHARMA better resembles the satellite observations of Sandu et al. (2010) than SAM does during the SCT (Fig. 3k in de Roode et al., 2016), but that is not necessarily proof of model skill since case study large-scale forcings tend to be insufficiently constrained by available observations (e.g.,
485 Vogelmann et al. 2015). The detailed dynamical and microphysical differences between the models warrants further investigation, and future observational studies are necessary to provide firmer foundation of the impact of absorbing aerosol on the timing of SCT.

Our study suggests that even in the case of a hastened transition an initially overlying absorbing aerosol layer can produce a net negative aerosol indirect and semi-
490 direct radiative forcings during SCT. For lightly drizzling stratocumulus, such negative forcing is mainly attributable to greater cloud albedo from a dominant Twomey effect and to negative LW forcing from greater cloud breakup over warmer SSTs and reduced PBL top height from aerosol heating. Diminishing already from the interactions between microphysical and semi-direct processes, when combined with aerosol direct SW forcing,
495 the net SW forcing nearly vanishes, and therefore less significant relative to the negative LW forcing during the SCT. We recommend that such sizable LW forcings not be neglected when considering semi-direct aerosol forcings in the context of stratocumulus breakup. Further sensitivity tests (Appendix A1) show that when SSA at 0.5- μm wavelength decreases further, the negative contributions can be overcome by the large
500 positive SW forcing via direct absorption, leading to net positive aerosol forcings. We find it likely that similar positive forcings occur with an increase of aerosol layer thickness.



When the aerosol layer is initially placed at a higher altitude, the extended duration of aerosol overriding the stratocumulus deck intensifies the positive SW forcing 505 from direct absorption, while largely enhancing the negative SW indirect and semi-direct forcings from less LWP reduction owing to less entrained aerosol and a stronger inversion, leading to a more negative net forcing when averaged over the 3-day transition.

A moist layer aloft associated with outflow from a deeper continental PBL tends to intensify the radiative forcings by reducing cloud-top LW cooling and thus convective 510 intensity and increasing the positive SW forcing before contact with the PBL, and by enhancing negative SW forcing after contact via greater LWP resulting from reduced PBL drying. The net effect of the overlying additional moisture is to modestly increase cloud water during the 3-day transition. Absorbing aerosol in the presence of additional moisture tends to break up the cloud more dramatically relative to the effect of absorbing 515 aerosol without additional moisture aloft. The presence of moisture little affects the LW forcing but leads to substantially more net downward SW flux at TOA. Averaged over the 3-day transition, the positive SW forcing cancels out the negative LW forcing.

We note that the simulations in this study are derived from observations over the northeast Pacific Ocean (Sandu et al., 2010) whereas the characteristics of the overlying 520 absorbing aerosol layer are based on observations from the southeast Atlantic (A15). The different large-scale meteorological conditions at these two locations may limit the generality of this study to the SCT over the Atlantic. However, we find it likely that similarly complex interactions (as summarized in Table 3) do occur. Future modeling studies based on conditions over the southeast Atlantic should be developed to evaluate 525 the results presented here and in Y15. This study may help inform future analyses



primarily by emphasizing the complexity of competing LW and SW effects, and giving some indication of their relative strengths, which lead to a wide range of indirect plus semi-direct forcings from slightly positive to -20 W m^{-2} over our 3-day simulations, depending upon assumptions made (Tables 1, 8, 9, and A1). The duration of time before 530 the absorbing aerosol layer makes contact with the PBL, the strength of drizzle prior to contact, the number concentration of aerosol entrained after contact and the amount of moisture accompanying the aerosol are all found to be factors of leading potential importance to regional radiative impacts of biomass burning over the southeast Atlantic and elsewhere.

535

Acknowledgments. This research was funded by the NASA ORACLES project and the DOE ASR program. Resources supporting this work were provided by the NASA High-End Computing (HEC) Program through the NASA Advanced Supercomputing (NAS) Division at Ames Research Center. We thank Paquita Zuidema for helpful 540 suggestions.

APPENDIX

a. Sensitivity of cloudiness and aerosol radiative forcing to SSA and initial number concentration

Fig. A1 compares the 3-day transition with varying values of SSA (at $0.55\text{-}\mu\text{m}$ wavelength) for the absorbing aerosol. As discussed earlier, the microphysical effect of aerosol acts to greatly reduce cloud water and hasten the SCT by virtue of an enhanced entrainment. This effect is also seen in the “SSA=1” case (pure scattering aerosol) in Fig. A1. The increased entrainment is reflected by the fact that the deepening of the PBL



varies little from the baseline simulation, despite substantially reduced cloud cover and
550 LWP. A decrease of SSA from 1 to 0.88 serves to strengthen the inversion and enhance
the diurnal cycle. These trends are greater when SSA is further reduced to 0.71, which
strengthens the inversion by ~3 K on day 2 and ~4 K on day 3, and deepens the PBL 400
m less by the end of day 3. The strengthened inversion slightly hinders cloud breakup,
while still hastening the SCT relative to the baseline (Figs. A1b and A1c). Although the
555 decrease of SSA amplified the net negative LW forcing via the slower deepening of the
PBL, that LW forcing is more than offset by the positive SW forcing attributable to direct
absorption by the aerosol, and therefore the 3-day mean radiative forcing increases with
the decrease of SSA. Thus, for the strongly absorbing aerosol case (SSA = 0.71) it is seen
in Table A1 that the net radiative forcing is positive on average.

560 The radiative forcing is also sensitive to the initial number concentration of the
overlying aerosol, as a five-fold reduction in $N_{a, \text{absorb}}$, to 1000 mg^{-1} , leads to the average
radiative forcing nearly vanishing during the transition (Table A1).

565 **b. Combined effects of overlying absorbing aerosol in the absence of
sedimentation and evaporation effects**

As seen in Fig. A2, an overlying absorbing aerosol results in a delayed SCT when
570 sedimentation and evaporation effects are both omitted. The lack of microphysical
effects on dynamics isolates the influence of aerosol heating, which increases LWP
and especially cloud cover during the night and delays the SCT. We note that Y15
also found a delay in the SCT, but the similarity with this result may be coincidental.



REFERENCES

- 575 Abdul-Razzak, H., & Ghan, S. J. (2000). A parameterization of aerosol activation 2. Multiple aerosol types. *J. Geophys. Res.*, 105, 6837-6844.

Albrecht, B. A. (1989). Aerosols, cloud microphysics, and fractional cloudiness. *Science*, 245(4923), 1227-1230.

580 Ackerman, A. S., Toon, O. B., & Hobbs, P. V. (1993). Dissipation of marine stratiform clouds and collapse of the marine boundary layer due to the depletion of cloud condensation nuclei by clouds. *Science*, 262(5131), 226-229.

Ackerman, A. S., Toon, O. B., Stevens, D. E., Heymsfield, A. J., Ramanathan, V., & Welton, E. J. (2000). Reduction of tropical cloudiness by soot. *Science*, 288(5468), 1042-1047.

Ackerman, A. S., Kirkpatrick, M. P., Stevens, D. E., & Toon, O. B. (2004). The impact of humidity above stratiform clouds on indirect aerosol climate forcing. *Nature*, 432(7020), 1014-1017.

585 Ackerman, A.S., M.C. van Zanten, B. Stevens, V. Savic-Jovicic, C.S. Bretherton, A. Chlond, J.-G. Golaz, H. Jiang, M. Khairoutdinov, S.K. Krueger, D.C. Lewellen, A. Lock, C.-H. Moeng, K. Nakamura, M.D. Petters, J.R. Snider, S. Weinbrecht, and M. Zulauf, 2009: Large-eddy simulations of a drizzling, stratocumulus-topped marine boundary layer. *Mon. Weather Rev.*, 137, 1083-1110.

Adebiyi, A. A., Zuidema, P., & Abel, S. J. (2015). The convolution of dynamics and moisture with the presence of shortwave absorbing aerosols over the southeast Atlantic. *J. Clim.*, 28, 1997-2024.

590 Bretherton, C. S., & Wyant, M. C. (1997). Moisture transport, lower-tropospheric stability, and decoupling of cloud-topped boundary layers. *Journal of the Atmospheric Sciences*, 54(1), 148-167.

Bretherton, C. S., Blossey, P. N., & Uchida, J. (2007). Cloud droplet sedimentation, entrainment efficiency, and subtropical stratocumulus albedo. *Geophysical Research Letters*, 34(3).

595 Chand, D., Wood, R., Anderson, T. L., Satheesh, S. K., & Charlson, R. J. (2009). Satellite-derived direct radiative effect of aerosols dependent on cloud cover. *Nature Geoscience*, 2(3), 181-184.



- Coakley, J. A., Jr., & Walsh, C. D. (2002). Limits to the aerosol indirect radiative effect derived from
600 observations of ship tracks. *J. Atmos. Sci.*, 59, 668-680.
- Cook, J., & Highwood, E. J. (2004). Climate response to tropospheric absorbing aerosols in an intermediate
general-circulation model. *Quarterly Journal of the Royal Meteorological Society*, 130(596), 175-
191.
- de Lozar, A., and J. Mellado, 2016: Reduction of the entrainment velocity by
605 cloud droplet sedimentation in stratocumulus. *J. Atmos. Sci.* doi:10.1175/JAS-D-
16-0196.1, in press.
- de Roode, S. R., Sandu, I., van der Dussen, J. J., Ackerman, A. S., Blossey, P., Jarecka, D., ... & Stevens,
B. (2016). Large eddy simulations of EUCLIPSE/GASS Lagrangian stratocumulus to cumulus
transitions: Mean state, turbulence, and decoupling. *Journal of the Atmospheric Sciences*, (2016).
- 610 Engelhart, G. J., Hennigan, C. J., Miracolo, M. A., Robinson, A. L., & Pandis, S. N. (2012). Cloud
condensation nuclei activity of fresh primary and aged biomass burning aerosol. *Atmospheric
Chemistry and Physics*, 12(15), 7285-7293.
- Feingold, G., Jiang, H., & Harrington, J. Y. (2005). On smoke suppression of clouds in Amazonia.
Geophysical Research Letters, 32(2).
- 615 Forster, A., Schouten, S., Baas, M., & Damsté, J. S. S. (2007). Mid-Cretaceous (Albian–Santonian) sea
surface temperature record of the tropical Atlantic Ocean. *Geology*, 35(10), 919-922.
- Geoffroy, O., Brenguier, J.-L., & Burnet, F. (2010). Parametric representation of the cloud droplet spectra
for LES warm bulk microphysical schemes. *Atmos. Chem. Phys.*, 10, 4835-4848.
- Ghan, S. J. (2013). Technical Note: Estimating aerosol effects on cloud radiative forcing. *Atmospheric
Chemistry and Physics*, 13(19), 9971-9974.
- 620 Hansen, J., Sato, M., & Ruedy, R. (1997). Radiative forcing and climate response. *Journal of Geophysical
Research: Atmospheres*, 102(D6), 6831-6864.
- Haywood, J., Francis, P., Dubovik, O., Glew, M., & Holben, B. (2003a). Comparison of aerosol size
distributions, radiative properties, and optical depths determined by aircraft observations and Sun
625 photometers during SAFARI 2000. *Journal of Geophysical Research: Atmospheres*, 108(D13).



Haywood, J., Osborne, S. R., Francis, P. N., Keil, A., Formenti, P., Andrae, M. O., & Kaye, P. H. (2003b).

The mean physical and optical properties of regional haze dominated by biomass burning aerosol measured from the C-130 aircraft during SAFARI 2000. *Journal of Geophysical Research: Atmospheres*, 108(D13).

630 Hindman, E. E., Porch, W. M., Hudson, J. G., & Durkee, P. A. (1994). Ship-produced cloud lines of 13 July 1991. *Atmospheric Environment*, 28(20), 3393-3403.

Jacobson, M. Z. (2002). Control of fossil-fuel particulate black carbon and organic matter, possibly the most effective method of slowing global warming. *Journal of Geophysical Research: Atmospheres*, 107(D19).

635 Johnson, B. T., Shine, K. P., & Forster, P. M. (2004). The semi-direct aerosol effect: Impact of absorbing aerosols on marine stratocumulus. *Quarterly Journal of the Royal Meteorological Society*, 130(599), 1407-1422.

Johnson, B. T. (2005). Large-eddy simulations of the semidirect aerosol effect in shallow cumulus regimes. *Journal of Geophysical Research: Atmospheres*, 110(D14).

640 Keil, A., & Haywood, J. M. (2003). Solar radiative forcing by biomass burning aerosol particles during SAFARI 2000: A case study based on measured aerosol and cloud properties. *Journal of Geophysical Research: Atmospheres*, 108(D13).

Khairoutdinov, M. F., & Randall, D. A. (2003). Cloud resolving modeling of the ARM summer 1997 IOP: Model formulation, results, uncertainties, and sensitivities. *Journal of the Atmospheric Sciences*, 60(4), 607-625.

Klein, S. A., & Hartmann, D. L. (1993). The seasonal cycle of low stratiform clouds. *Journal of Climate*, 6(8), 1587-1606. Morrison, H., Curry, J. A., & Khvorostyanov, V. I. (2005). A new double-moment microphysics parameterization for application in cloud and climate models. Part I: Description. *Journal of the Atmospheric Sciences*, 62(6), 1665-1677.

650 Labonne, M., Bréon, F. M., & Chevallier, F. (2007). Injection height of biomass burning aerosols as seen from a spaceborne lidar. *Geophysical Research Letters*, 34(11).



Lindstrot, R., Stengel, M., Schröder, M., Fischer, J., Preusker, R., Steenbergen, T., & Bojkov, B. R. (2014).

A global climatology of total columnar water vapour from SSM/I and MERIS. *Earth. Sys. Sci. Data*, 6, 221-233.

655 Lohmann, U., & Feichter, J. (2001). Can the direct and semi-direct aerosol effect compete with the indirect effect on a global scale?. *Geophysical Research Letters*, 28(1), 159-161.

Menon, S., Hansen, J., Nazarenko, L., & Luo, Y. (2002). Climate effects of black carbon aerosols in China and India. *Science*, 297(5590), 2250-2253.

Morrison, H., Curry, J. A., & Khvorostyanov, V. I. (2005). A new double-moment microphysics parameterization for application in cloud and climate models. Part I: Description. *Journal of the Atmospheric Sciences*, 62(6), 1665-1677.

Morrison, H., & Grabowski, W. W. (2008). Modeling supersaturation and subgrid-scale mixing with two-moment bulk warm microphysics. *Journal of the Atmospheric Sciences*, 65(3), 792-812.

Penner, J. E., Zhang, S. Y., & Chuang, C. C. (2003). Soot and smoke aerosol may not warm climate. 665 *Journal of Geophysical Research: Atmospheres*, 108(D21).

Petters, M. D., & Kreidenweis, S. M. (2007). A single parameter representation of hygroscopic growth and cloud condensation nucleus activity. *Atmospheric Chemistry and Physics*, 7(8), 1961-1971.

Pincus, R., & Baker, M. B. (1994). Effect of precipitation on the albedo susceptibility of clouds in the marine boundary layer. *Nature*, 372(6503), 250-252.

670 Randall, D. A., Coakley Jr, J. A., Lenschow, D. H., Fairall, C. W., & Kropfli, R. A. (1984). Outlook for research on subtropical marine stratification clouds. *Bulletin of the American Meteorological Society*, 65(12), 1290-1301.

Sakaeda, N., Wood, R., & Rasch, P. J. (2011). Direct and semidirect aerosol effects of southern African biomass burning aerosol. *Journal of Geophysical Research: Atmospheres*, 116(D12).

675 Sandu, I., Brenguier, J. L., Geoffroy, O., Thouron, O., & Masson, V. (2008). Aerosol impacts on the diurnal cycle of marine stratocumulus. *Journal of the Atmospheric Sciences*, 65(8), 2705-2718.

Sandu, I., Stevens, B., & Pincus, R. (2010). On the transitions in marine boundary layer cloudiness. *Atmospheric Chemistry and Physics*, 10(5), 2377-2391.



Sandu, I., & Stevens, B. (2011). On the factors modulating the stratocumulus to cumulus transitions.

680 *Journal of the Atmospheric Sciences*, 68(9), 1865-1881.

Slingo, A., & Schrecker, H. M. (1982). On the shortwave radiative properties of stratiform water clouds.

Quarterly Journal of the Royal Meteorological Society, 108(456), 407-426.

Stevens, B., Cotton, W. R., Feingold, G., & Moeng, C.-H. (1998). Large eddy simulations of strongly precipitating, shallow, stratocumulus-topped boundary layers. *Journal of the Atmospheric Sciences*,

685 55, 3616-3638.

Toon, O. B., McKay, C. P., Ackerman, T. P., & Santhanam, K. (1989). Rapid calculation of radiative heating rates and photodissociation rates in inhomogeneous multiple scattering atmospheres. *J. Geophys. Res.*, 94(D13), 16287-16301.

Twomey, S. (1974). Pollution and the planetary albedo. *Atmospheric Environment*, 8(12), 1251-1256.

690 Twomey, S. (1991). Aerosols, clouds and radiation. *Atmospheric Environment. Part A. General Topics*, 25(11), 2435-2442.

Vogelmann, A.M., A.M. Fridlind, T. Toto, S. Endo, W. Lin, J. Wang, S. Feng, Y. Zhang, D.D Turner, Y. Liu, Z. Li, S. Xie, A.S. Ackerman, M. Zhang, & M. Khairoutdinov (2015). RACORO continental boundary layer cloud investigations. Part I: Case study development and ensemble large-scale forcings. *J. Geophys. Res. Atmos.*, 120(12), 5962-5992, doi:10.1002/2014JD022713.

695 Wyant, M. C., Bretherton, C. S., Rand, H. A., & Stevens, D. E. (1997). Numerical simulations and a conceptual model of the stratocumulus to trade cumulus transition. *Journal of the Atmospheric Sciences*, 54(1), 168-192.

Wood, R. (2007). Cancellation of aerosol indirect effects in marine stratocumulus through cloud thinning. *J. Atmos. Sci.* 64, 2657-2779.

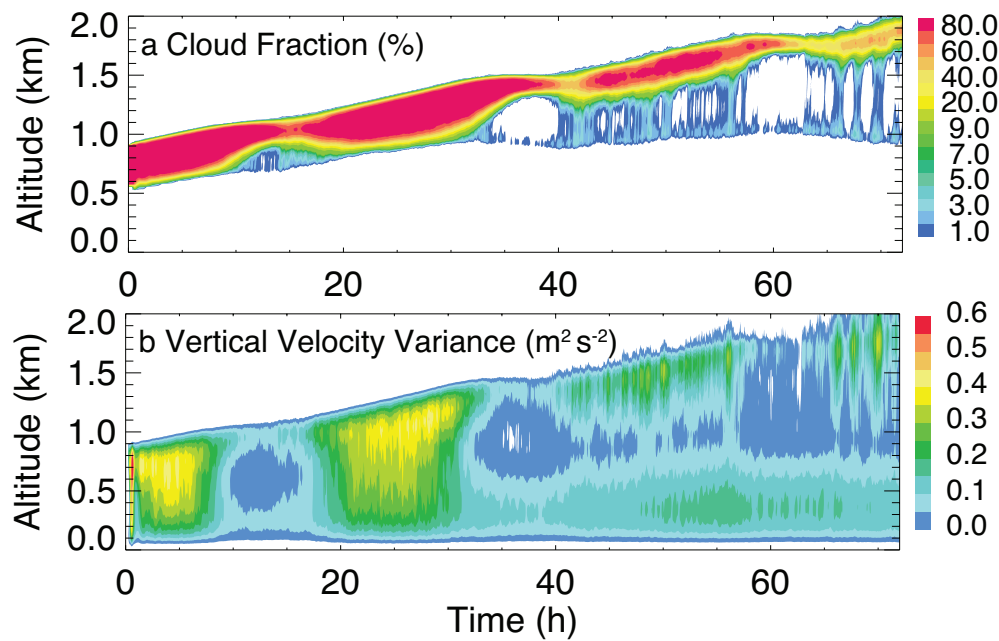
700 Xue, H., Feingold, G., & Stevens, B. (2008). Aerosol effects on clouds, precipitation, and the organization of shallow cumulus convection. *Journal of the Atmospheric Sciences*, 65(2), 392-406.

Yamaguchi, T., Feingold, G., Kazil, J., & McComiskey, A. (2015). Stratocumulus to cumulus transition in the presence of elevated smoke layers. *Geophysical Research Letters*, 42(23).

705 Zhou, X., Kollas, P., & Lewis, E. R. (2015). Clouds, precipitation, and marine boundary layer structure during the MAGIC field campaign. *Journal of Climate*, 28(6), 2420-2442.



FIGURES



710 Fig. 1. Evolution of horizontal average profiles of (a) cloud fraction (where cloud water
711 mixing ratio exceeds 0.01 g kg^{-1}) and (b) vertical velocity variance for lightly drizzling
712 baseline case ($N_{\text{a, sulfate}} = 150 \text{ mg}^{-1}$).

715

720

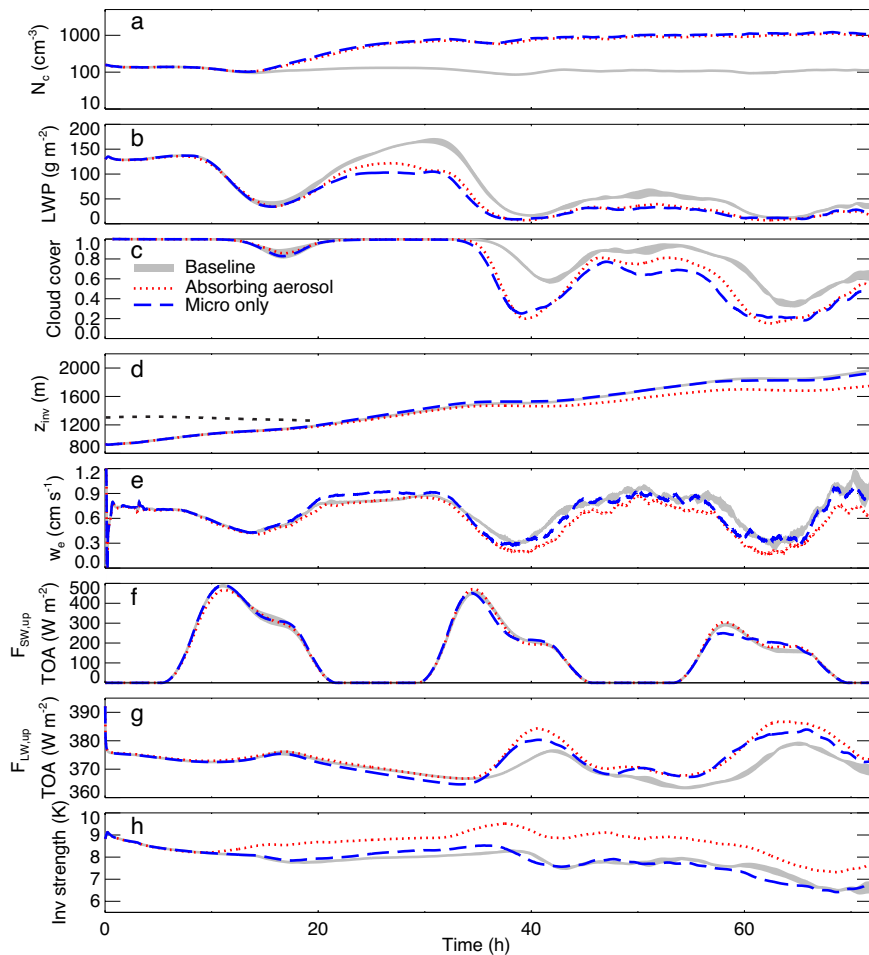


Fig. 2. Evolution of domain averages of (a) cloud droplet number concentration (N_c , average weighted by cloud water mixing ratio), (b) liquid water path (LWP), (c) cloud cover (columns with $LWP > 10 \text{ g m}^{-2}$), (d) inversion height (height of maximum potential temperature gradient), (e) entrainment rate (difference of inversion height tendency and subsidence rate at inversion height), (f) upwelling shortwave (SW) and (g) longwave (LW) radiative fluxes at TOA and (h) inversion strength (ΔT across inversion defined as



the vertical extent with continuous positive temperature gradient). Results shown as
730 lagged 3-hour running averages to smooth entrainment rates. Range of 3-member lightly
drizzling baseline ensemble ($N_{a, \text{sulfate}} = 150 \text{ mg}^{-1}$) in gray. Results with absorbing aerosol
layer shown as red dotted line. Aerosol layer excluding radiative interaction shown as
blue dashed line. The black dotted line in (d) indicates the base of absorbing aerosol layer
(lowest height where $N_{a, \text{absorb}}$ is full strength) before contacting the boundary layer.

735

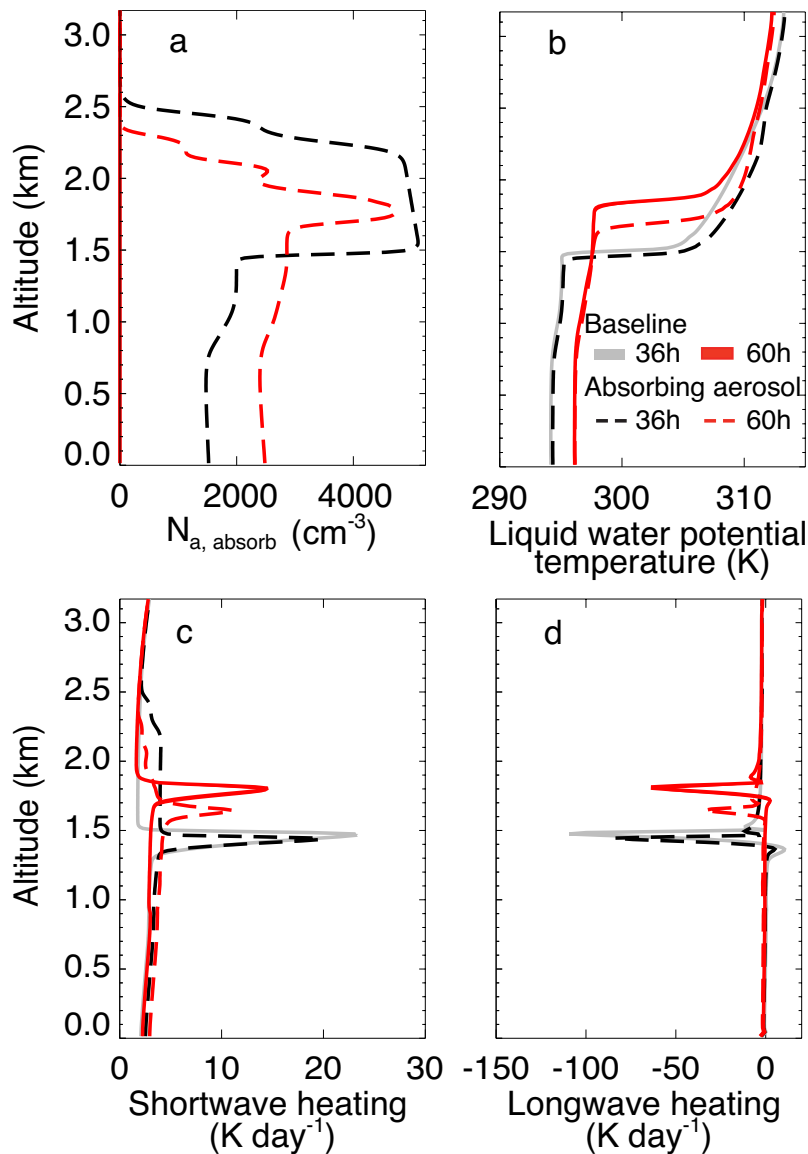


Fig. 3. Horizontally averaged profiles of (a) number concentration of absorbing aerosol, (b) liquid water potential temperature, (c) SW heating rate and (d) LW heating rate at 36th hour (gray solid line) and 60th hour (red solid line) for lightly drizzling baseline ensemble ($N_{a, \text{sulfate}} = 150 \text{ mg}^{-1}$) and with overlying absorbing aerosol (dashed line).

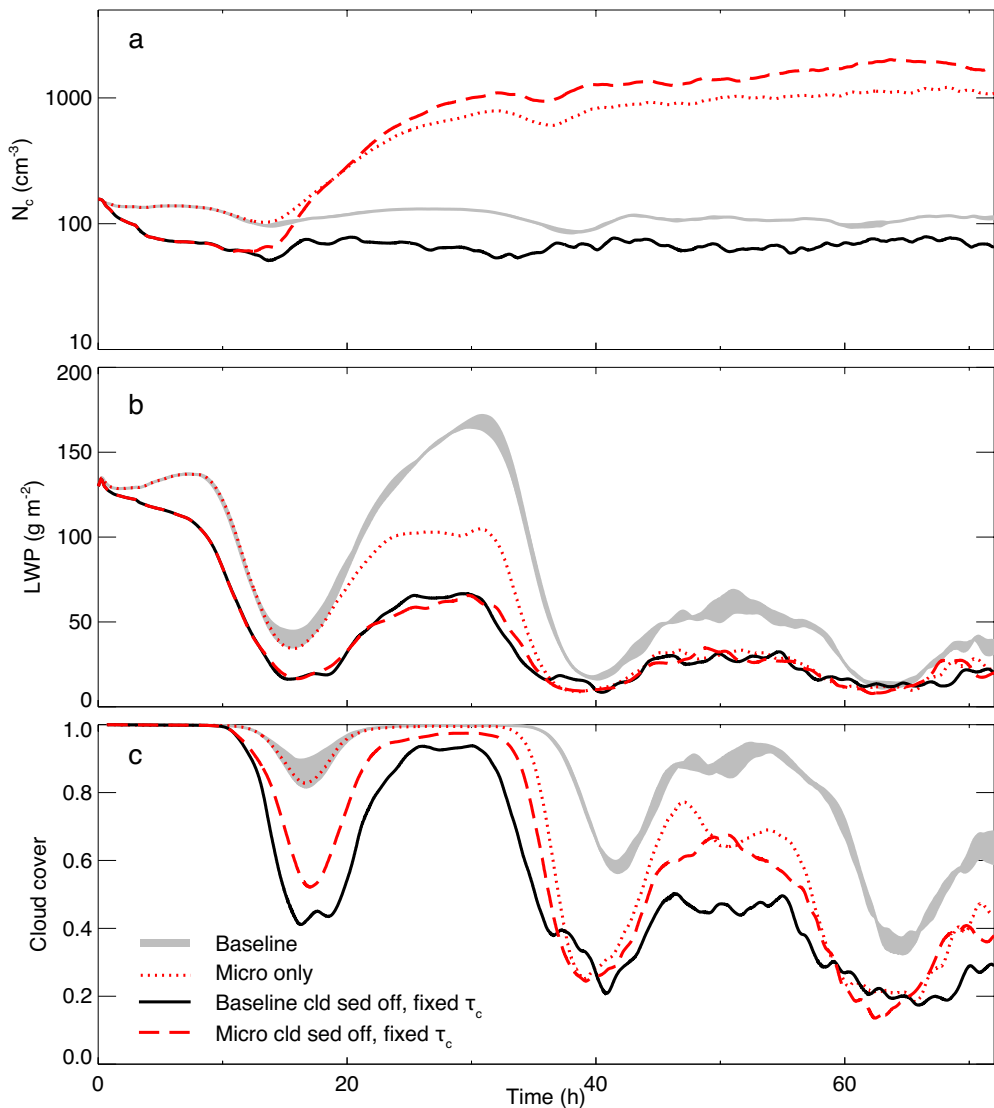


Fig. 4. As in Fig. 2 with baseline in gray and with overlying aerosol that does not affect radiation shown with dotted red line. Baseline and overlying aerosol cases in the absence 745 of cloud-droplet sedimentation and with the relaxation time for diffusional growth of cloud droplet (τ_c) fixed are shown with black solid and red dashed lines respectively.

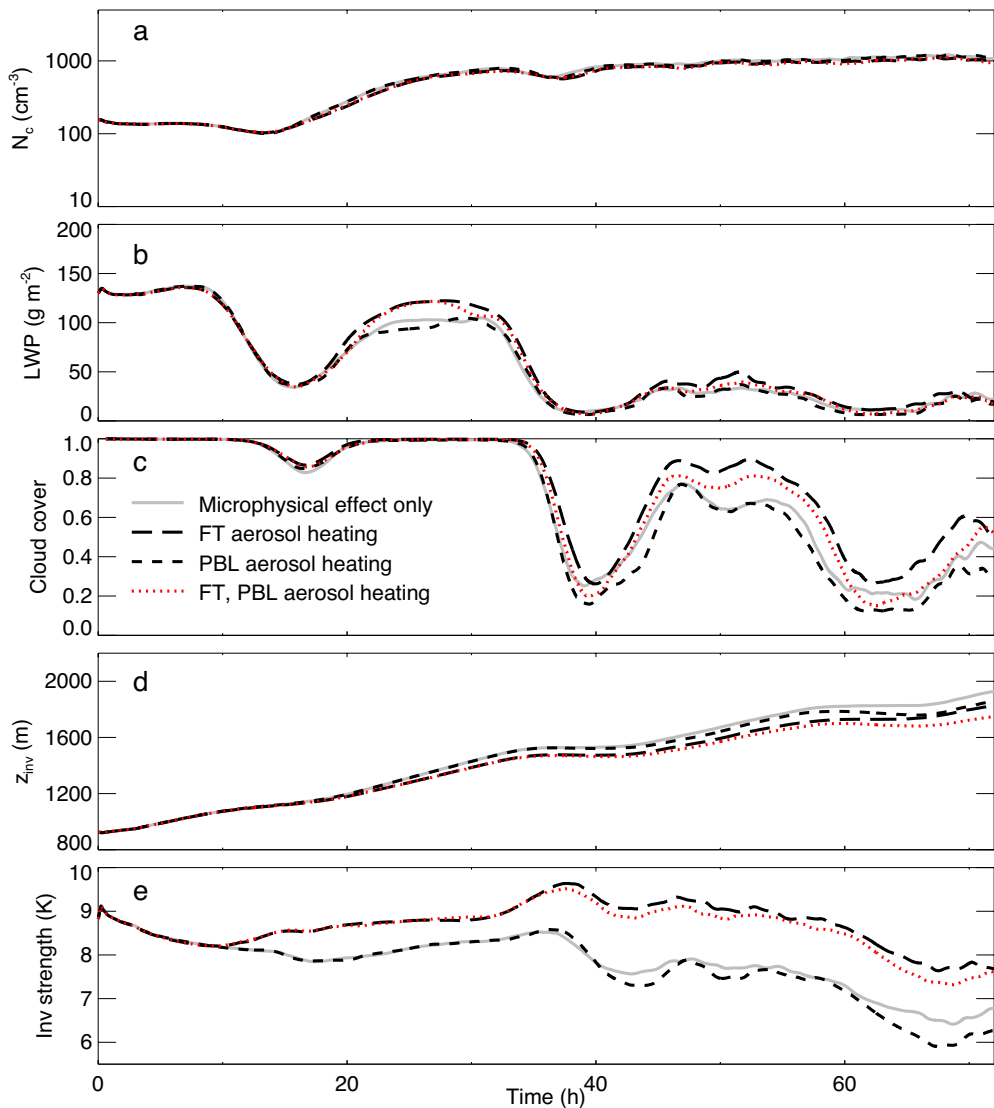
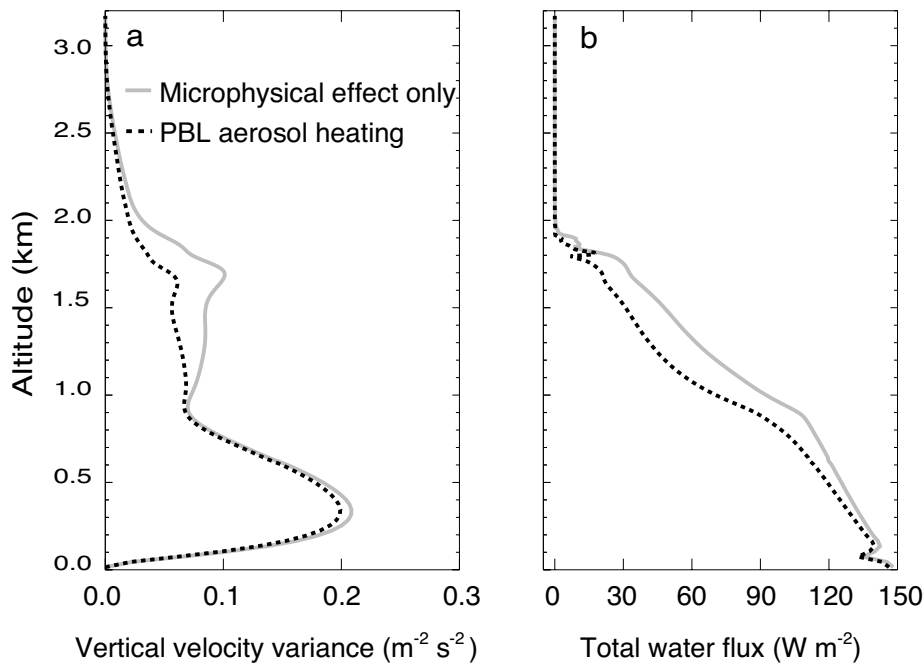


Fig. 5. As in Fig. 2. All cases include initially overlying absorbing aerosol and allow them to act as CCN. For gray solid line the aerosol does not affect radiation. For long and short dashed lines, the aerosol affects radiation only in the free troposphere (FT) and planetary boundary layer (PBL), respectively. For red dotted line there are no restrictions on aerosol affecting radiation, as in Fig. 2.



755 Fig. 6. Horizontally averaged profiles of (a) vertical velocity variance and (b) total water flux averaged over 10 AM to 2 PM local time on day 3 for simulations with and without absorbing aerosol affecting radiation in the PBL. Both simulations include microphysical effects.

760

765

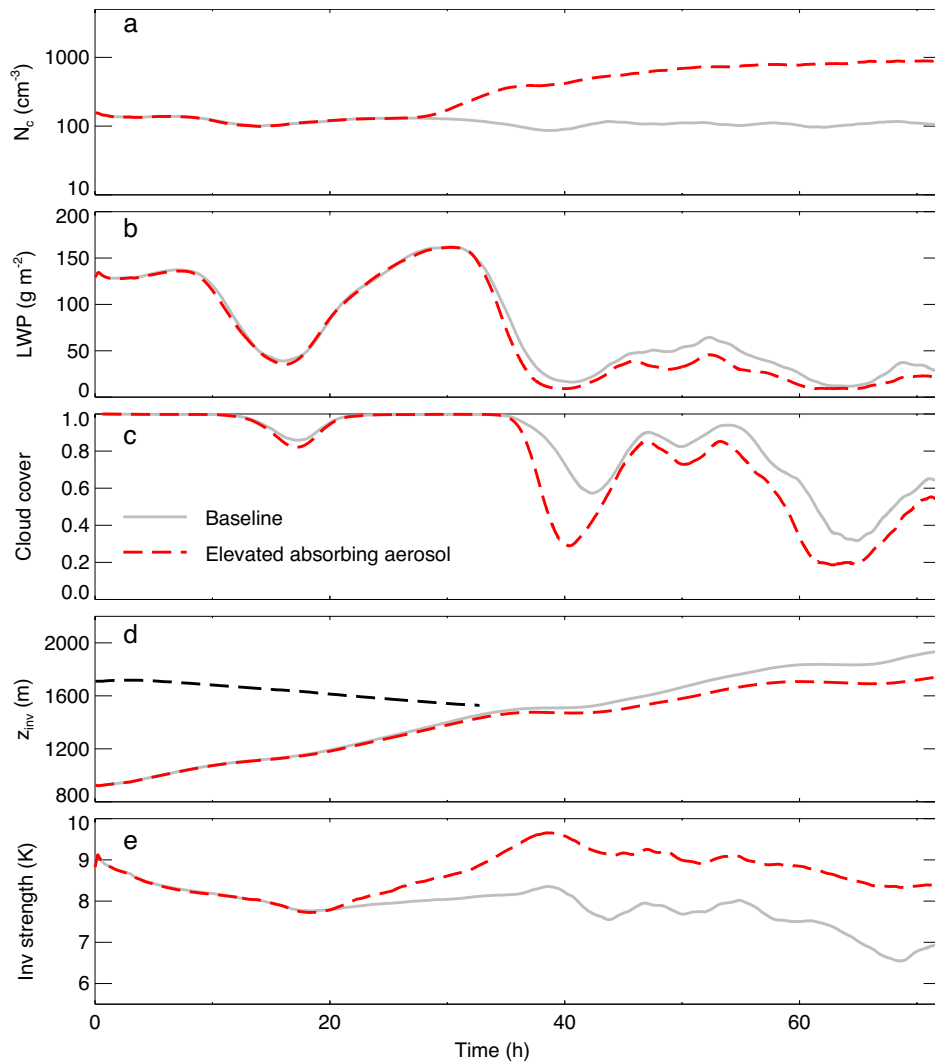
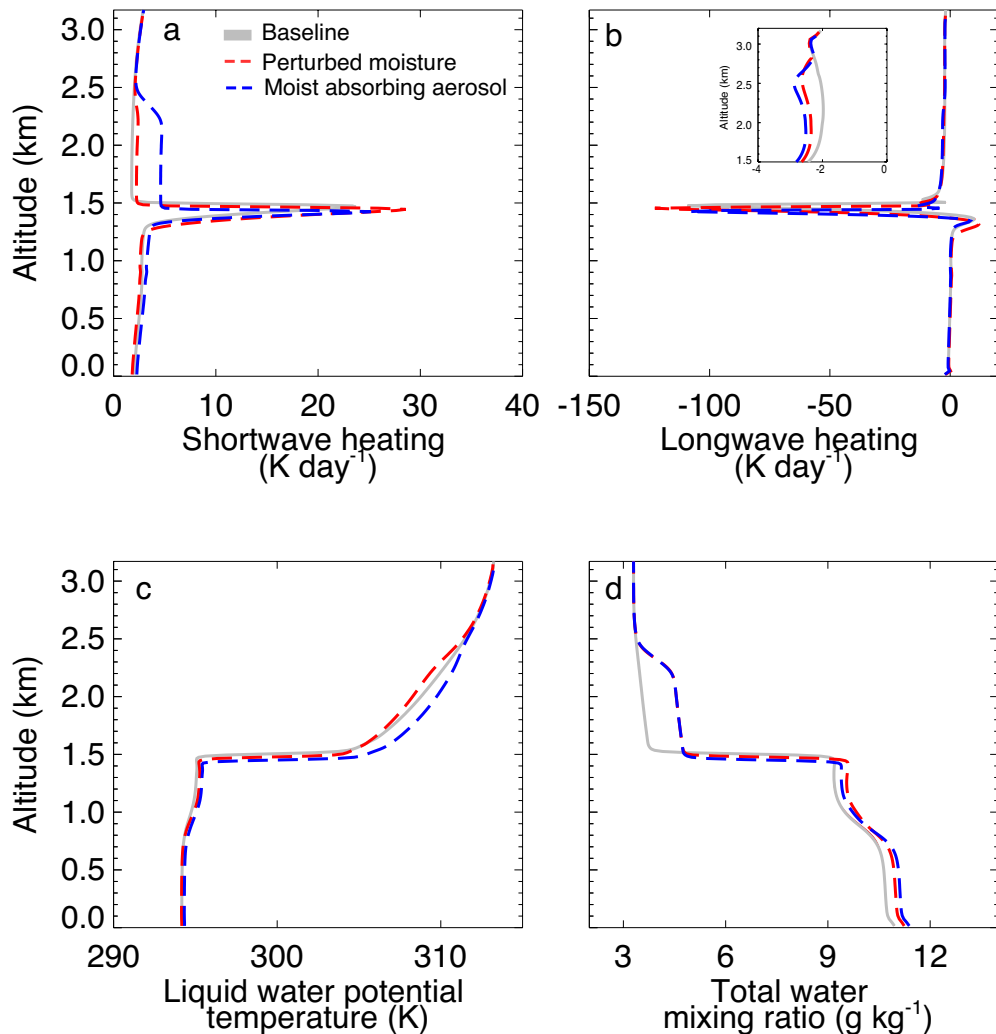


Fig. 7. As in Fig. 2. The baseline with a 3.5-km deep grid (N_a , sulfate=150 mg^{-1}) in gray.

770 Results with aerosol layer initially 400 m higher shown as red dashed line, with corresponding aerosol layer base shown as black dashed line in (d).



775

Fig. 8. Horizontally averaged profiles of (a) SW heating rate, (b) LW heating rate, (c) liquid water potential temperature, and (d) total water mixing ratio averaged over hours 35-37 for lightly drizzling baseline ensemble ($N_{a, \text{sulfate}} = 150 \text{ mg}^{-1}$) (gray and black), perturbed moist case (red), and perturbed moist absorbing aerosol case (blue). The sub 780 panel in (b) shows diurnal-average LW heating rate on day 1 from 1.5 to 3.2 km for the above three cases.

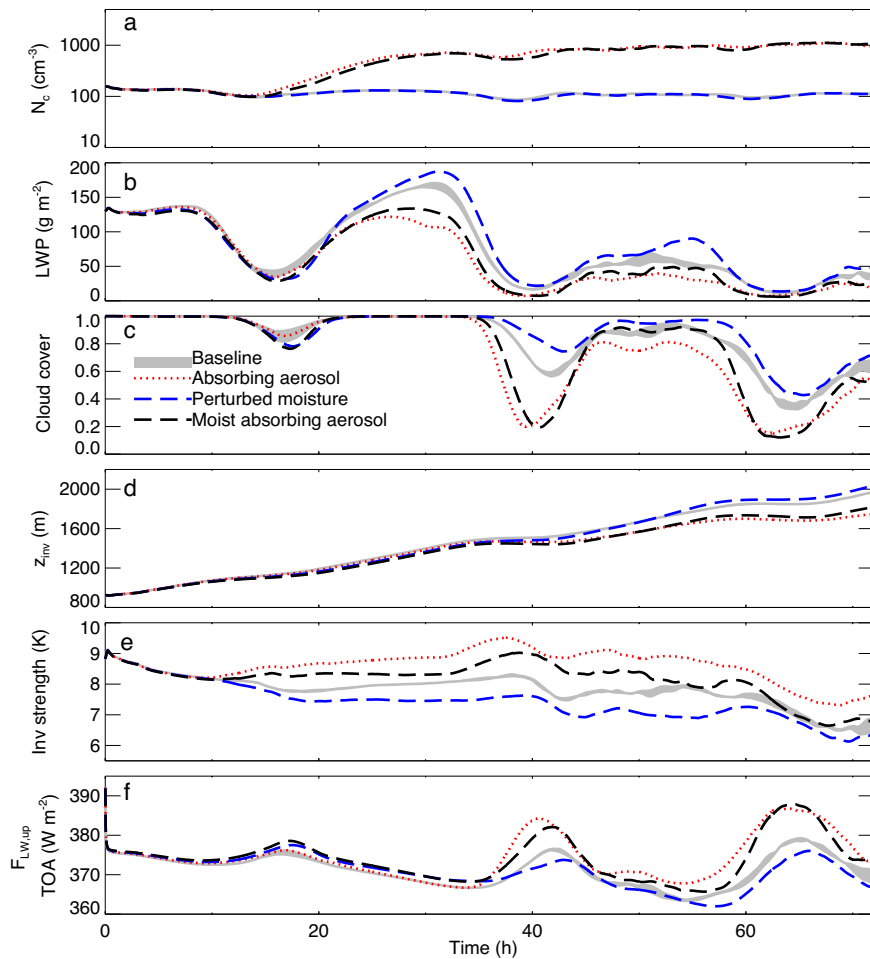


Fig. 9. As in Fig. 2. Range of three-member lightly drizzling baseline ensemble (N_a ,
 785 $\text{sulfate} = 150 \text{ mg}^{-1}$) shown in gray. Results with absorbing aerosol layer shown as red dotted
 line. Baseline with moist layer aloft shown with blue dashed line. Results with moist
 absorbing aerosol shown as black dashed line.

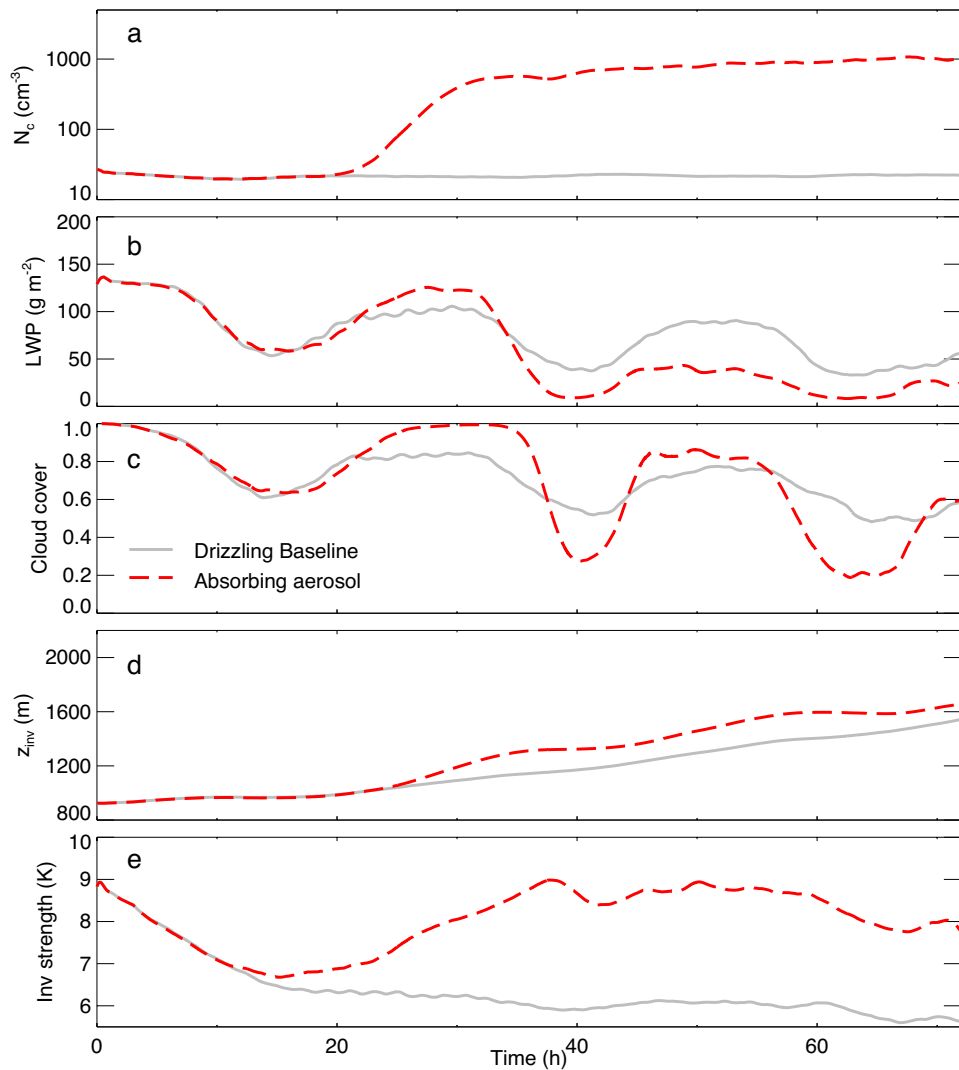


Fig. 10. As in Fig. 2 but for heavily drizzling baseline ($N_{\text{a, sulfate}} = 25 \text{ mg}^{-1}$) and with
795 absorbing aerosol layer with the same $N_{\text{a, sulfate}}$.

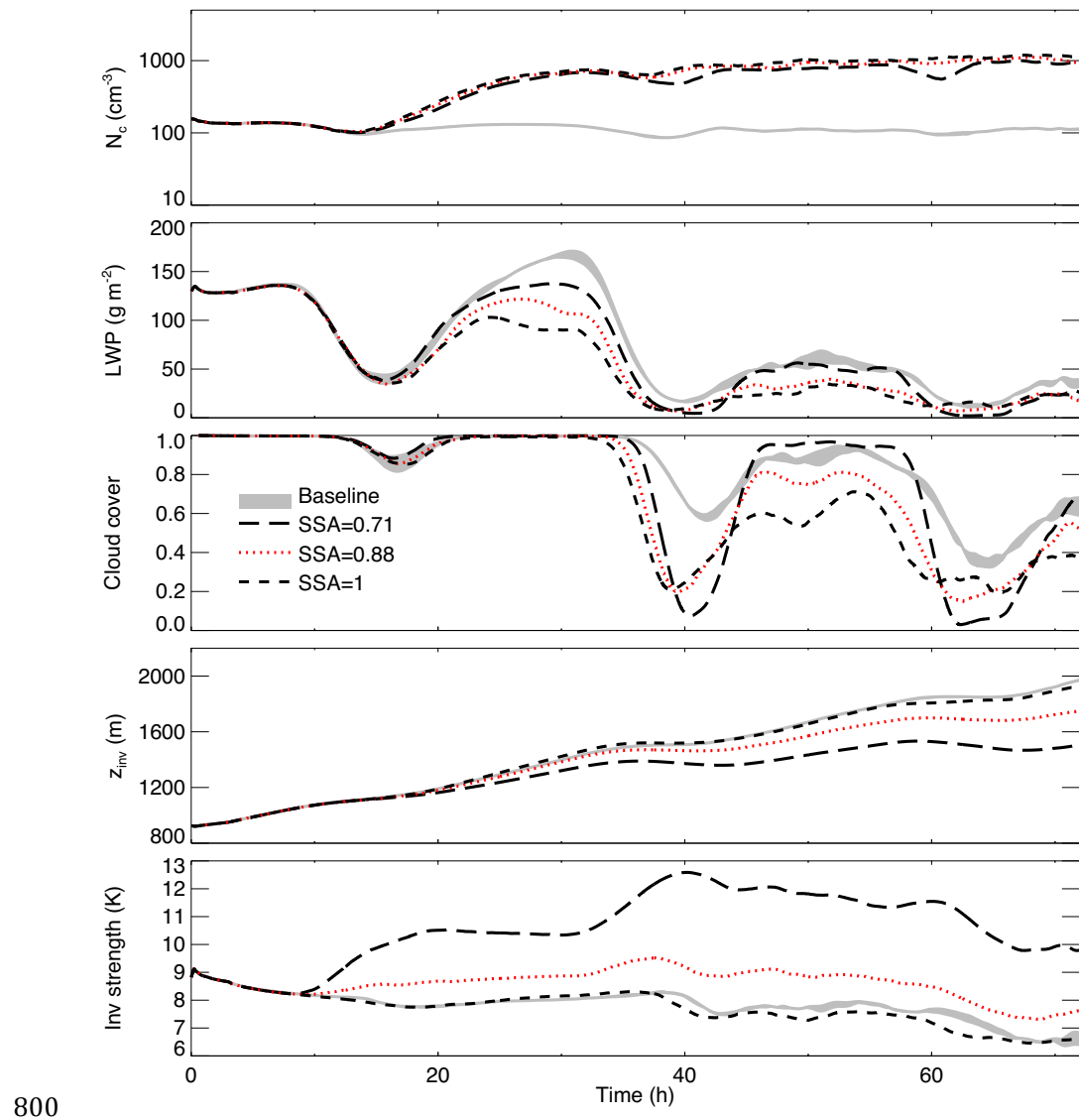
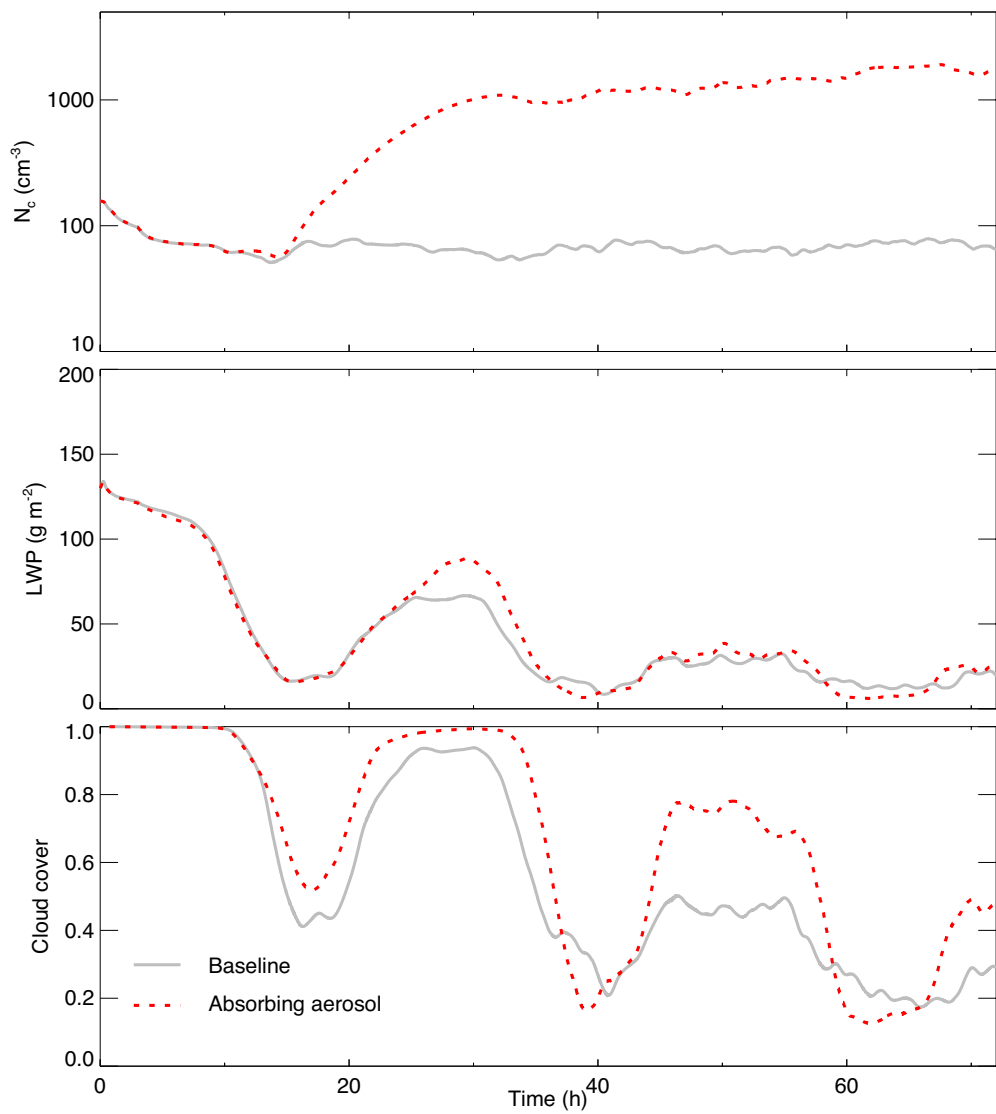


Fig. A1. As in Fig. 2. Range of three-member lightly drizzling baseline ensemble (N_a , sulfate = 150 mg⁻¹) in gray. Varying single scattering albedo (SSA) of absorbing aerosol as given in legend.



805

Fig. A2. As in Fig. 2 but for lightly drizzling baseline and with absorbing aerosol in the absence of sedimentation and evaporation effects.

810



TABLES

Table 1. Diurnal-average direct forcing, indirect and semi-direct forcings, and all forcings (in W m^{-2}) from the overlying absorbing aerosol for the lightly drizzling case (N_a , 815 $\text{sulfate} = 150 \text{ mg m}^{-3}$) on days 1 (0-24 h), day 2 (24-48 h) and day 3 (48-72 h). The three-day average radiative forcing is indicated in the last row. Boldface indicates results exceeding the uncertainty range derived from the baseline ensemble spread.

	Direct forcing			Indirect, semi-direct forcings			All forcings
	SW	LW	SW+LW	SW	LW	SW+LW	SW+LW
Day 1	7.3	-0.3	7.0	-1.6	-0.2	-1.8	5.2
Day 2	0.8	-0.2	0.6	-0.5	-2.6	-3.1	-2.5
Day 3	-3.7	0.0	-3.7	-1.2	-6.0	-7.2	-10.9
Mean	1.5	-0.2	1.3	-1.1	-2.9	-4.0	-2.7

820

825



Table 2. Diurnal-average changes in cloud radiative forcings (ΔCRF ; in W m^{-2}) of the overlying absorbing aerosol case relative to the lightly drizzling baseline case ($N_{\text{a, sulfate}}=150 \text{ mg}^{-1}$). Conventions as in Table 1.

830

$\Delta\text{CRF TOA} (\text{W m}^{-2})$			
	SW	LW	SW+LW
Day 1	14.6	-0.2	14.4
Day 2	8.5	-2.0	6.5
Day 3	2.3	-4.8	-2.5
Mean	8.4	-2.3	6.1

835

840



Table 3. Indirect forcing of absorbing aerosol, computed as the diurnal-average difference in radiative fluxes at TOA (in W m^{-2}) of the simulation with absorbing aerosol not affecting radiation, relative to the lightly drizzling baseline case ($N_{\text{a, sulfate}}=150 \text{ mg}^{-1}$).

845 Conventions as in Table 1.

Indirect forcing			
	SW	LW	SW+LW
Day 1	-0.7	0.4	-0.3
Day 2	2.5	-0.9	1.6
Day 3	1.2	-5.2	-4.0
Mean	1.0	-1.9	-0.9

850

855



Table 4. Schematic of SW and LW radiative responses (changes in net downward fluxes
 860 at TOA) to microphysical and thermal effects of initially overlying absorbing aerosol
 layer. N_c refer to cloud-droplet concentrations, CF cloud fraction, and Z_i inversion height.

	SW	LW
Microphysical effects		
Twomey effect	$N_c \uparrow$	-
Cloud-droplet sedimentation \downarrow	$CF \downarrow$	+
Evaporation \uparrow		-
FT aerosol heating		
Inversion strength \uparrow	$CF \uparrow$	-
	$Z_i \downarrow$	-
PBL aerosol heating		
Aerosol heating	$CF \downarrow$	+
RH decrease	$Z_i \downarrow$	-
Other		
Warming SST		-



Table 5. Semi-direct forcing of absorbing aerosol, computed as the diurnal-average difference in radiative fluxes at TOA (in W m^{-2}) of simulations with aerosol heating restricted to the FT, PBL, or not restricted, relative to the simulation without aerosol heating. All simulations allow the absorbing aerosol to act as CCN. Boldface indicates results exceeding the uncertainty range derived from the spread of the lightly drizzling baseline ensemble.

Semi-direct forcing				
		SW	LW	SW+LW
FT aerosol heating	Day 1	-1.9	-0.6	-2.5
	Day 2	-12.4	-0.2	-12.6
	Day3	-20.6	2.7	-17.9
PBL aerosol heating	Day 1	-1.3	0.0	-1.3
	Day 2	5.5	-1.2	4.3
	Day3	15.2	-3.2	12.0
FT, PBL aerosol heating	Day 1	-0.9	-0.6	-1.5
	Day2	-3.0	-1.7	-4.7
	Day3	-2.4	-0.8	-3.2
	Mean	-2.1	-1.0	-3.1



870 Table 6. As in Table 1 but with absorbing aerosol layer initially located 400 m higher.

Boldface indicates results exceeding the uncertainty range derived from the spread of the lightly drizzling baseline ensemble.

	Direct forcing			Indirect, semi-direct forcings			All forcings
	SW	LW	SW+LW	SW	LW	SW+LW	SW+LW
Day 1	6.5	-0.2	6.3	4.2	-0.6	3.6	9.9
Day 2	3.8	-0.3	3.5	-11.2	-1.9	-13.1	-9.6
Day 3	-3.0	-0.1	-3.1	-5.0	-4.7	-9.7	-12.8
Mean	2.4	-0.2	2.2	-4.0	-2.4	-6.4	-4.2

875

880



885 Table 7. As in Table 1 but for the response of a lightly drizzling baseline to a perturbation
of moisture instead of aerosol.

	TOA (W m ⁻²)		
	SW	LW	SW+LW
Day 1	11.6	-1.3	10.3
Day 2	-17.5	-0.2	-17.7
Day 3	-9.9	2.4	-7.2
Mean	-5.2	0.3	-4.9

890

895

900



Table 8. As in Table 1 but for a lightly drizzling baseline with a moisture perturbation aloft. Boldface indicates results exceeding the uncertainty range derived from the spread of the lightly drizzling baseline ensemble.

Direct forcing				Indirect, semi-direct forcings			All forcings
	SW	LW	SW+LW	SW	LW	SW+LW	SW+LW
Day 1	6.1	-0.2	5.9	-1.5	-0.3	-1.8	4.1
Day 2	1.8	-0.2	1.6	3.0	-2.2	0.8	2.4
Day 3	-3.5	0.0	-3.6	2.8	-6.8	-4.0	-7.6
Mean	1.5	-0.1	1.4	1.4	-3.1	-1.7	-0.3

905

910

915



Table 9. As in Table 8 but for a heavily drizzling baseline ($N_{a, \text{sulfate}} = 25 \text{ mg}^{-1}$).

Direct forcing				Indirect, semi-direct forcings			All forcings
	SW	LW	SW+LW	SW	LW	SW+LW	SW+LW
Day 1	0.3	-0.1	0.2	-0.5	0.0	-0.5	-0.3
Day 2	2.0	-0.2	1.8	-52.0	6.3	-45.7	-43.9
Day 3	-3.4	-0.0	-3.4	-9.4	3.4	-6.0	-9.4
Mean	-0.4	-0.1	-0.5	-20.6	3.2	-17.4	-17.9

920

925

930



Table A1. As in Table 1 but for absorbing aerosol with different values of single scattering albedo (SSA), and only showing averages over the three-day transition. For the last case the aerosol loading is reduced five-fold.

$N_{a,\text{absorb}} (\text{mg}^{-1})$	Direct forcing			Indirect, semi-direct			All forcings	
	SW	LW	SW+LW	SW	LW	SW+LW	SW+LW	
5000	SSA=0.71	15.9	-0.2	15.7	-5.1	-5.2	-10.3	5.4
	SSA=0.88	1.5	-0.2	1.3	-1.1	-2.9	-4.0	-2.7
	SSA=1.00	-4.9	-0.1	-5.0	0.8	-2.5	-1.7	-6.7
1000	SSA=0.88	0.2	0.0	0.2	2.5	-1.9	0.6	0.8